PROCEEDINGS of the
24th International Congress on Acoustics

October 24 to 28, 2022 in Gyeongju, Korea

ABS-0244

A spherical beamforming algorithm for acoustic centering and phase correction of source directivities

Samuel D. BELLOWS[1]; Timothy W. LEISHMAN[2]

[1,2] Brigham Young University, USA

ABSTRACT

The directivities of acoustic sources have many applications in auralizations, room acoustical designs, and sound source modeling. Of practical importance in directivity measurements is the location of the source's acoustic center relative to the array's geometric center. The authors recently developed an acoustic source centering algorithm based on the equivalence of far-field magnitude directivity patterns of centered and uncentered directivities. This work explores how the far-field phase directivity patterns likewise lead to source-centering procedures. While the phase-based algorithm is less robust than the magnitude-based approach, the technique is notable for its significant improvements in computational efficiency. The paper provides algorithm validations with both theoretical sources and measured trumpet directivities.

Keywords:

1. INTRODUCTION

The directivity of a sound source characterizes the spatial dependence of its acoustic radiation over frequency. Understanding the directional characteristics of sources has broad applications, including auralizations, room acoustical design, microphone placement, and source modeling. Directivity measurements are typically performed by sampling at a constant-radius spherical surface with a specified sampling density, such as the 5 or 10-degree angular resolution suggested by the AES sampling standard (1). Of practical concern when measuring the directivity of a source is the location of the source relative to the geometric center of the microphone array. Source misalignment within the array can lead to several undesirable effects. First, the measured pressure on the array surface may not be representative of the desired far-field directivity pattern (2). Additionally, source translations increase the number of expansion terms required, which in turn increase the likelihood of spatial aliasing (3, 4). Thus, proper source positioning within the array is essential for practical directivity measurements.

More recently, the authors have shown that in the far-field, the magnitude pattern of centered and translated sources are equivalent (5). One can exploit this equivalence to determine the reference frame from which the near-field pattern converges most rapidly to the known far-field magnitude pattern. While this approach is robust at higher frequencies and useful for complex sources, its computational expense is limiting because the formulation requires extraction of magnitude patterns in the spatial domain rather than an efficient spherical-harmonic-based process. To improve upon these limitations, this work presents an acoustic centering algorithm based on a source's far-field phase patterns. The relations between the far-field phases of centered and translated sources can cast the acoustic centering problem as the detection of arrival (DOA) of a local plane-wave with efficient solutions using spherical-harmonic-domain beamforming. Theoretical results help validate the robustness of the approach, and the technique successfully centers measured trumpet directivities.

[1] samuel.bellows11@gmail.com
[2] tim_leishman@byu.edu

2. ALGORITHM

2.1 Far-field Phase Relationship

Consider an acoustic source radiating into free space. If a closed spherical surface of radius $r = a$ entirely encompasses the source, the exterior solution to the Helmholtz equation in spherical coordinates yields the pressure for $r \geq a$ (6):

$$p(r,\theta,\phi,k) = \sum_{n=0}^{\infty}\sum_{m=-n}^{n} c_n^m(k) h_n^{(2)}(kr) Y_n^m(\theta,\phi), \tag{1}$$

where k is the wavenumber, $h_n^{(2)}(kr)$ are the spherical Hankel functions of the second kind of order n, $Y_n^m(\theta,\phi)$ are the normalized spherical harmonics of degree n and order m, and $c_n^m(k)$ are the frequency-dependent expansion coefficients. Exploiting the orthogonality of the spherical harmonics over the sphere yields the expansion coefficients:

$$c_n^m(k) = \frac{1}{h_n^{(2)}(ka)} \int_0^{2\pi}\int_0^{\pi} p(a,\theta,\phi,k)[Y_n^m(\theta,\phi)]^* sin\theta d\theta d\phi, \tag{2}$$

where * indicates complex conjugation. In the acoustic and geometric far-field of the source, where $kr >> 1$ and $r >> d$, with d being the spatial extent of the source, the asymptotic form of the spherical Hankel functions simplifies Eq. (1) to the form

$$p(r,\theta,\phi,k) \approx \frac{e^{-ikr}}{kr} \sum_{n=0}^{\infty}\sum_{m=-n}^{n} c_n^m i^{n+1} Y_n^m(\theta,\phi). \tag{3}$$

The far-field simplification allows separation of the pressure field's angular and radial dependence, yielding an unnormalized directivity function

$$\widetilde{D}(\theta,\phi,k) \approx \sum_{n=0}^{\infty}\sum_{m=-n}^{n} c_n^m i^{n+1} Y_n^m(\theta,\phi). \tag{4}$$

Next, one may assume that the source has an acoustic center and let $D_c(\theta,\phi,k)$ denote its far-field normalized directivity function with the origin of the coordinate system aligned with the acoustic center. One may further let $D(\theta,\phi,k)$ denote the sources' far-field directivity function measured with the acoustic center located at position $\boldsymbol{r_c}$. The first directivity product theorem then relates these two directivity functions as (5, 6)

$$D(\theta,\phi,k) = e^{ik\mathbf{r_c}\cdot\hat{\mathbf{r}}} D_c(\theta,\phi,k), \tag{5}$$

where $\hat{\mathbf{r}}$ is the unit vector in the direction of $\boldsymbol{r}$. This key result shows that in the far-field, the magnitude directivity patterns of the centered and uncentered source are equivalent. However, the phase shift factor $e^{ik\mathbf{r_c}\cdot\hat{\mathbf{r}}}$ between the centered and uncentered patterns remains. Figure 1 illustrates this shift through color-mapped far-field phase spheres for a monopole, dipole, and radially vibrating cap set on a rigid sphere. Each constant-radius plot describes the phase of the pressure using a cyclical color scheme. Figures 1(a), 1(d), and 1(g) show the far-field phase of each source when aligned with the array center. For the case of the vibrating cap on a sphere, the center of the sphere aligns with the array center. Next, Figs. 1(b), 1(e), and 1(h) show the far-field phase for each source after a translation of $\mathbf{r_c}$ = (0.0, 0.1, 0.3) m. Finally, Figs. 1(c), 1(f), and 1(i) show the difference in phase pattern between the translated and untranslated cases. The numerical results verify that regardless of how simple or complex the initial phase of an untranslated source may be, the phase difference depends only on the translation and wavenumber as described in Eq. (5).

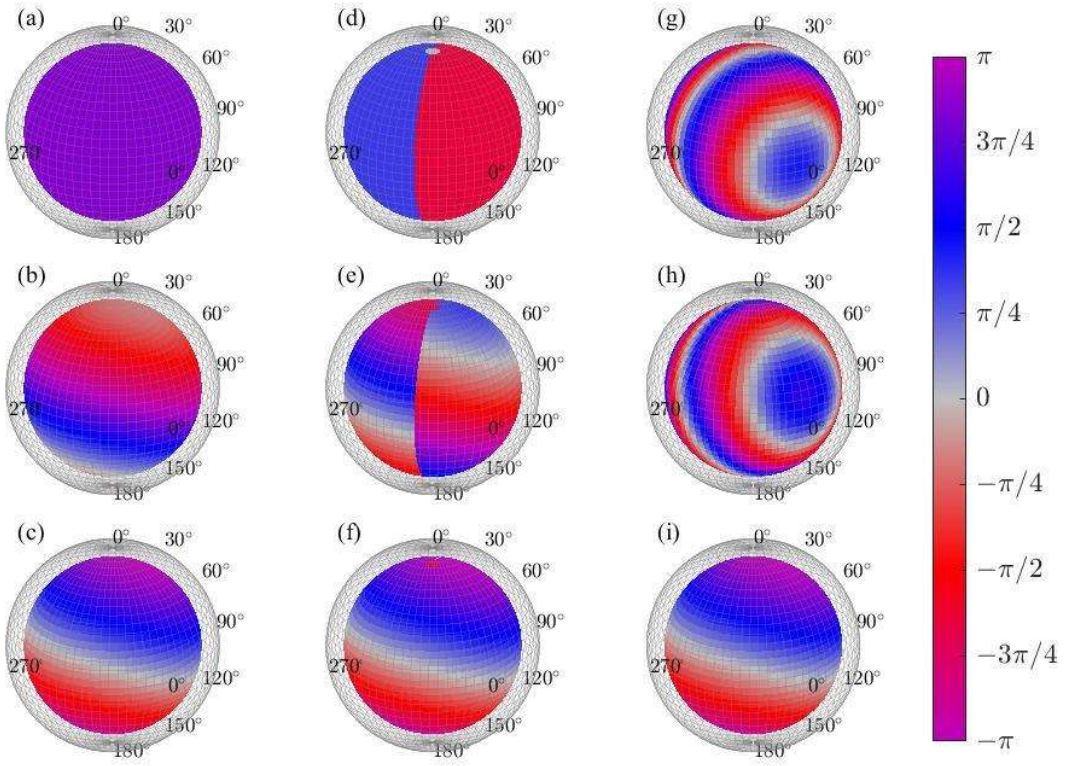

Figure 1 – Far-field phase spheres for a monopole [(a)-(c)], dipole [(d)-(f)], and radially vibrating cap on a sphere [(g)-(i)]. These include cases for the sources located at the center of the measurement array [(a), (d), and (g)], translated to position (0.0, 0.1, 0.3) m [(b), (e), and (h)], and the phase differences between the untranslated and translated sources [(c), (f), and (i)].

2.2 Phase-based Centering Algorithm

Previous work exploited the equivalence of the far-field directivity magnitudes to develop a centering algorithm that is robust even at high frequencies and for complex sources (5). However, a disadvantage of the algorithm is that its use of magnitude patterns produces a computationally expensive approach in the spatial domain. This section leverages phase relationships between far-field directivities to yield a more computationally efficient algorithm with less robustness.

To begin with, for some sources one may assume that the phase of the centered pattern is roughly constant so that the measured far-field phase of the translated source is

$$\Psi(\theta, \phi, k) \approx k\boldsymbol{r_c} \cdot \hat{\boldsymbol{r}}. \tag{6}$$

The pressure of a unit-amplitude plane wave is

$$p(r, \theta, \phi, k) = e^{-i\boldsymbol{k}\cdot\boldsymbol{r}} = e^{-ir\boldsymbol{k}\cdot\hat{\boldsymbol{r}}}, \tag{7}$$

where **k** is the wavenumber vector with magnitude k, which points in the direction of propagation. By associating the term $k\boldsymbol{r_c}$ of the far-field phase with the $-r\boldsymbol{k}$ term of the plane wave, one may cast the acoustic centering problem as determining the direction of arrival (DOA) of the plane wave. One key difference between the two problems is that for the plane-wave DOA, r is typically known, so the steering need only be performed over the angular coordinates θ and ϕ. However, for the source centering problem, r_c is unknown; the varying radial positions require additional consideration.

A straightforward approach to the problem is to use a delay-and-sum beamformer. In this case one may let y be the output of the beamformer so that (7)

$$y = \boldsymbol{w}_{\boldsymbol{nm}}^{H}\boldsymbol{p}_{\boldsymbol{nm}}. \tag{8}$$

Here, $\boldsymbol{p}_{\boldsymbol{nm}}$ is a vector containing the spherical harmonic expansion coefficients of the far-field phase $e^{i\Psi}$ and $\boldsymbol{w}_{\boldsymbol{nm}}$ are the spherical harmonic coefficients of the beamforming weights,

$$w_{nm} = 4\pi \mathrm{i}^{\mathrm{n}} j_n(-kr)[\mathrm{Y}_{\mathrm{n}}^{\mathrm{m}}(\theta, \phi)]^*, \tag{9}$$

where j_n are the spherical Bessel functions of order n. The position $(r,\ \theta,\ \phi)$ that maximizes the beamformer output y is then the acoustic source center. Figure 2 illustrates this approach for a monopole located at r_c = 0.3 m and $(\theta_c, \phi_c) = (45°, 90°)$ with wavenumber k = 10 m^{-1}. Six different spherical projections for varying radial steering positions r_c show the beamformer output. The color scheme of each projection is kept constant to highlight that the acoustic center must be determined not only from the angular portion but also from the radial component. The beamformer's maximum output coincides with the monopole's true location, indicated by a red dot.

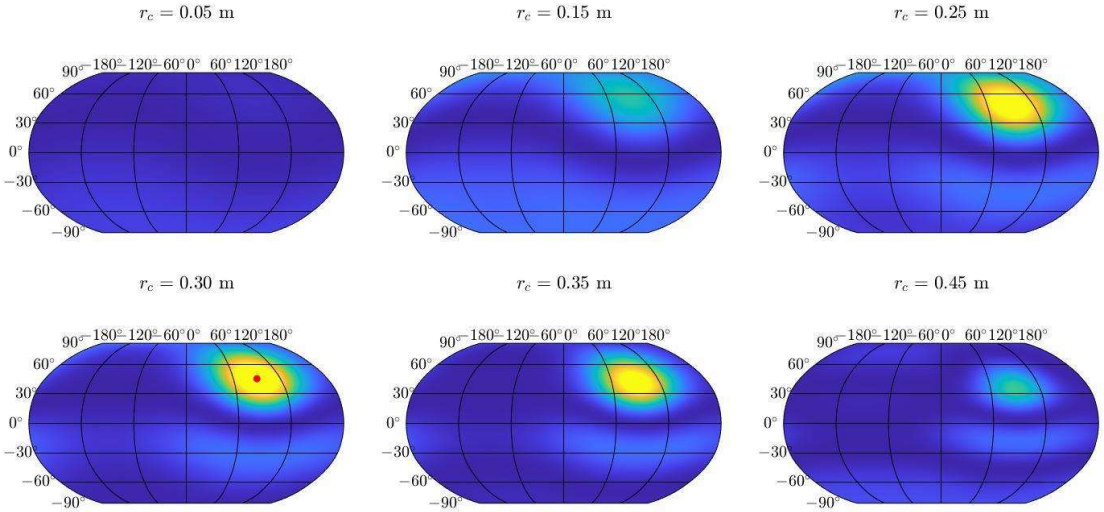

Figure 2 – Delay-and-sum beamformer output for the acoustic source centering problem.

While the formulation based on Eq. (8) provides a satisfactory result, one can further improve the algorithm's computational efficiency by noting the strong axial symmetry of the far-field phase as seen in Figs. 1(c), (f), and (i). Because the order m = 0 spherical harmonics are axially symmetric about $\hat{\boldsymbol{z}}$ for any degree n, the rotation of the far-field phase function that maximizes the energy in the p_n^0 coefficients can determine the direction in which $\hat{\boldsymbol{r}}_{\boldsymbol{c}}$ points. The Wigner-D rotation matrices $\mathbf{D}(\theta, \phi, \psi)$ allow this rotation to be carried out in the spherical harmonic domain (7). By letting

$$\boldsymbol{q}_{\boldsymbol{nm}}(\theta, \phi, \psi) = \boldsymbol{D}(\theta, \phi, \psi)\boldsymbol{p}_{\boldsymbol{nm}} \tag{10}$$

be the far-field phase spherical harmonic expansion coefficients after rotation, one finds that maximizing the objective function

$$J(\theta', \phi') = \sum_{n=0}^{\infty} |\boldsymbol{q}_{\boldsymbol{n0}}(\theta', \phi', 0)|^2 \tag{11}$$

yields the rotation required to orient the phase so that it is axially symmetric about $\hat{\boldsymbol{z}}$. Once this rotation is known, the direction (θ_c, ϕ_c) can be determined, and the delay-and-sum equation weights can be used with fixed angular components and varying radial components. The ambiguity in the rotation angle between $\hat{\boldsymbol{z}}$ and $-\hat{\boldsymbol{z}}$ resolves by allowing r_c to vary over both positive and negative ranges. Furthermore, because the degree n = 1 expansion terms contain the relevant directional

information for a single plane wave, the expansion coefficients $\boldsymbol{p_{nm}}$ may be truncated to a maximal $N = 1$ expansion, with the associated Wigner-D rotation matrices being of size 4 x 4 for increased computational efficiency.

3. THEORETICAL RESULTS

The dodecahedron regular polyhedron loudspeaker (RPL) is an interesting source to study because, even though it behaves much like a simple source at low frequencies, its directivity becomes complex at high frequencies (8). If one assumes the source has a single acoustic center, it must fall at the RPL center due to geometrical arguments. Thus, the RPL provides an ideal case of a complex radiator with a known acoustic center. Figure 3(a) shows the centered far-field phase of a simulated dodecahedron RPL for wavenumber $k = 30$ m^{-1} and RPL radius $a = 0.2$ m. Strong phase shifts are evident for each driver from the red patches in the general sphere of blue. Figure 3(b) shows the far-field phase after a source translation to $\mathbf{r_c} = (0.0, 0.1, 0.2)$ m. Figure 3(c) then shows the simplified phase using the degree $N = 1$ expansion, which correctly identifies the direction of translation.

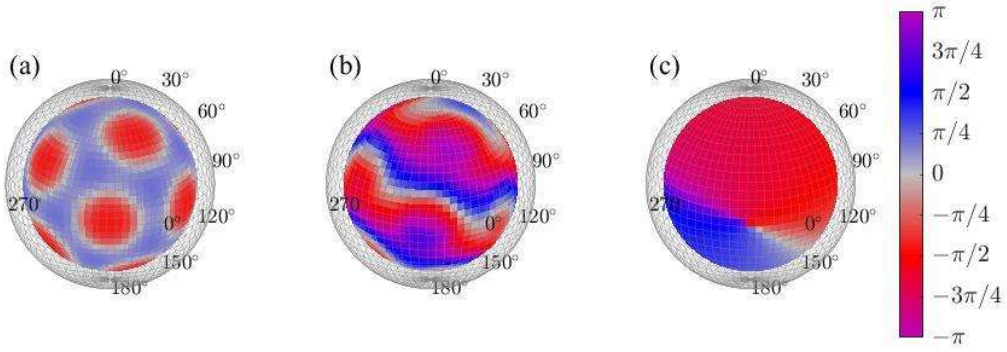

Figure 3 –Far-field color-mapped phase spheres for the (a) centered, (b) translated, and (c) translated dodecahedron using a simplified degree $N = 1$ expansion.

Figure 4 shows the centering results. The projected sphere plots the objective function $J(\theta', \phi')$ applied to the simplified phase shown in Fig. 3(c). The red dot indicates the true angular direction of the translation whereas the black × indicates the predicted direction. The line plot shows the delay-and-sum output using the identified direction and varying the radial parameter r_c. The vertical dashed red line indicates the true radial position.

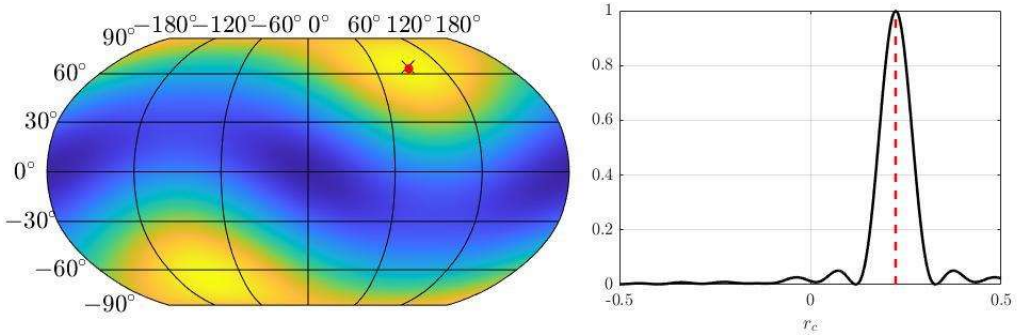

Figure 4 – Centering results for dodecahedral RPL. *Left:* Objective function $J(\theta', \phi')$. *Right*: normalized delay-and-sum output using a fixed angular position and varying r_c.

4. EXPERIMENTAL RESULTS

A radius a =1.17 m rotating semi-circular microphone array measured the directivity of a played trumpet with various mutes. The microphone array consisted of 36 12.7 mm (0.5") precision microphones that were relatively calibrated to a dedicated channel. The microphones were placed in 5° polar angle increments. Subsequent arc rotations in 5° azimuthal increments swept out a sphere with sampling density consistent with the AES standard on loudspeaker directivities (1), minus the

nadir (south pole) measurement position. A near-field reference microphone normalized varying excitation levels between the repeated measurements through frequency response functions (FRFs) as outlined in Ref. (9). A head restraint and laser mounted to the instrument restricted the musician's movements for greater consistency between measurements. Figure 5 shows the trumpet player within the measurement system.

Figure 5 – Trumpet player within measurement arc while playing with a cup mute.

Because of the small arc radius, placement the trumpet's bell close to the array's center was not practical. Consequently, the authors anticipated source misalignment between the instrument's acoustic center and the array's geometric center. Figure 6 shows the raw FRF-based directivity balloons with 1 Hz narrowband resolution for the first three partials of the note E4: 329 Hz, 658 Hz, and 988 Hz, respectively). Color and radius both depict levels on the surface of constant $r = a$, with the 0° marker indicating the direction in front of the musician. Figures 6(a)-(c) show the magnitude of the FRF-based balloon, whereas Figs. 6(d)-(f) show the phase. The magnitude balloons highlight the effectiveness of the FRF method, as the directivity functions show smoothly varying functions that reveal interesting directional characteristics, such as increasing diffraction lobes at higher frequencies. However, there appear to be reduced levels below the musician, likely due to the source placement within the array. The phase-based FRF-balloons validate this assertion, as similar patterns appear in Figs. 1 and 3(c).

Figures 6(g)-(i) show the far-field magnitude directivities after propagation via Eq. (3) using an $N = 34$ expansion, the maximal possible for the given sampling configuration. The directivity is much less directional, implying that many of the features evident in Figs. 6(a)-(c) are likely near-field effects. In addition, the principal axis of radiation lowers slightly.

The phase-based centering algorithm determined the acoustic center of each partial to be at (0.25, 0.00, 0.43) m, (0.25, 0.00, 0.42) m, and (0.29, 0.00, 0.34) m, respectively. While the acoustic center is generally considered to be frequency dependent, the position remains relatively consistent for the three partials. Figures 6(j)-(l) show the corresponding centered directivities of Figs. 6(a)-(c) based on expanding the pressure about the estimated acoustic center at a $a = 1.7$ m radius. Importantly, they show strong similarities with the far-field pattern, even though these are not far-field directivities. This result shows the effectiveness of the centering algorithm, as the pressure measured about the acoustic center should quickly converge to the far-field pattern (5). The area-weighted RMS deviation values (8) show that the deviations between the centered patterns of 6(j)-(l) and the far-field patterns of 6(g)-(i) were only 1.3, 1.7, and 2.0 dB compared to 1.9, 2.1, and 2.5 dB for the measured patterns of 6(a)-(c). Thus, the centering algorithm effectively reduces deviations between far-field directivities and nearer-field measurements.

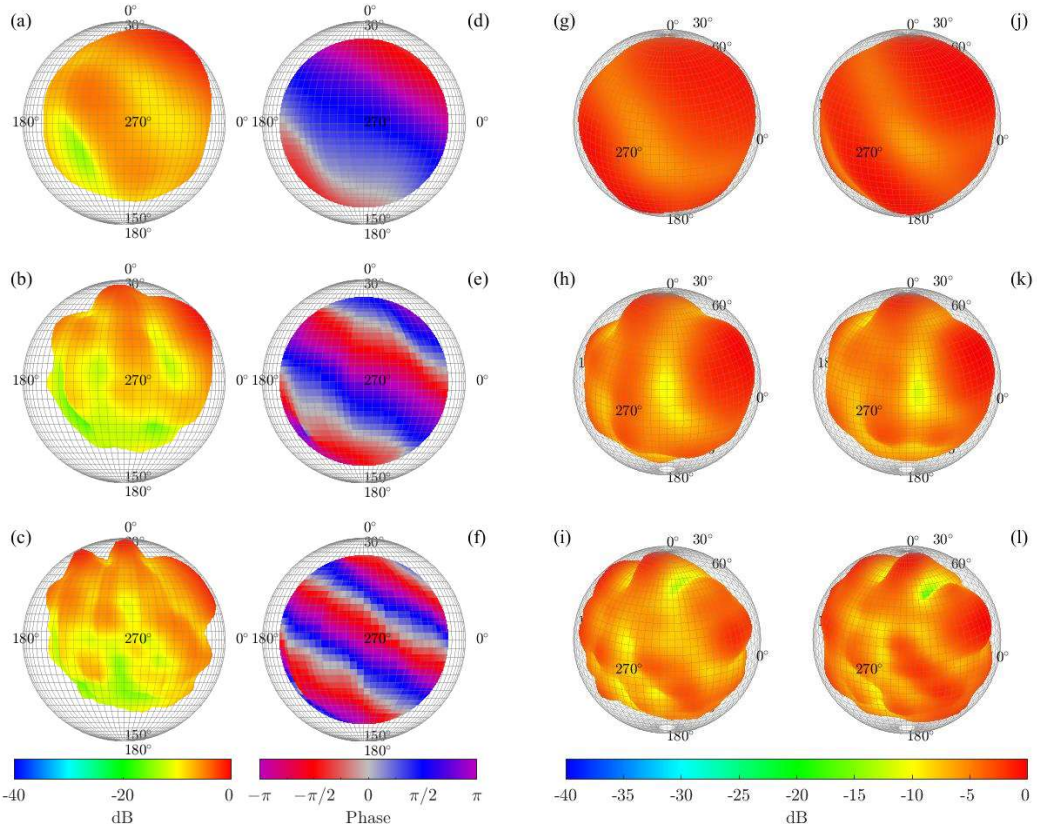

Figure – 6. Measured narrowband trumpet directivity patterns for the first [(a), (d), (g), and (j)], second [(b), (e), (h), and (k)] and third [(e), (f), (i), and (l)] partials. Figures (a)-(c) are FRF-based magnitude directivity patterns at the measurement surface. Figures (d)-(f) are the FRF-based phase patterns on the measurement surface. Figures (g)-(i) are the far-field magnitude patterns based on N=34 expansions. Figures (j)-(l) are the centered near-field magnitude patterns using the proposed algorithm.

5. CONCLUSIONS

This work has presented an acoustic centering algorithm based on the far-field phases of sources. It allows the acoustic centering problem to be reformulated in terms of a spherical beamforming problem. Theoretical directivities and measured musical instrument directivities validate the method. Future work could include the application of the algorithm to other sound sources and exploring other approaches for sources with more complex phase patterns.

ACKNOWLEDGEMENTS

This work was funded by the William James and Charlene Fuhriman Strong Family Musical Acoustics Endowed Fellowship.

REFERENCES

1. Audio Engineering Society. AES56-2008. AES Standard on Acoustics: Sound Source Modeling: Loudspeaker Polar Radiation Measurements. 2015.
2. Ureda MS. Apparent Apex Theory. Audio Engineering Society Convention 61, Paper 1403; 3-6 November 1978; New York, USA 1978. p. 1-15.
3. Deboy D. Acoustic centering and rotational tracking in surrounding spherical microphone arrays. [diploma thesis]. Graz: University of Music and Performing Arts Graz; 2010. 93 p.
4. Ben Hagai I, Pollow M, Vorländer M, Rafaely B. Acoustic centering of sources measured by surrounding spherical microphone arrays. J Acoust Soc Am. 2011;130(4):2003-2015.
5. Bellows SD, Leishman TW. Acoustic source centering of musical instrument directivities using acoustical

holography. Proc Meet Acous. 2020;42 055002.
6. Williams EG. Fourier Acoustics: Sound Radiation and Nearfield Acoustical Holography. London: Academic Press; 1999.
7. Rafaely B. Fundamentals of Spherical Array Processing. Berlin Heidelberg: Springer-Verlag; 2015.
8. Leishman TW, Rollins S, Smith HM. An experimental evaluation of regular polyhedron loudspeakers as omnidirectional sources of sound. J Acoust Soc Am. 2006;120(3):1411-1422.
9. Leishman TW, Bellows SD, Pincock CM, Whiting JK. High-resolution spherical directivity of live speech from a multiple-capture transfer function method. J Acoust Soc Am. 2021;149(3):1507-1523.